STRONG GROUND MOTION FROM EARTHQUAKES WITH MULTIPLE FAULTS

Ralph J. Archuleta, Chen Ji and Mareike N. Adams
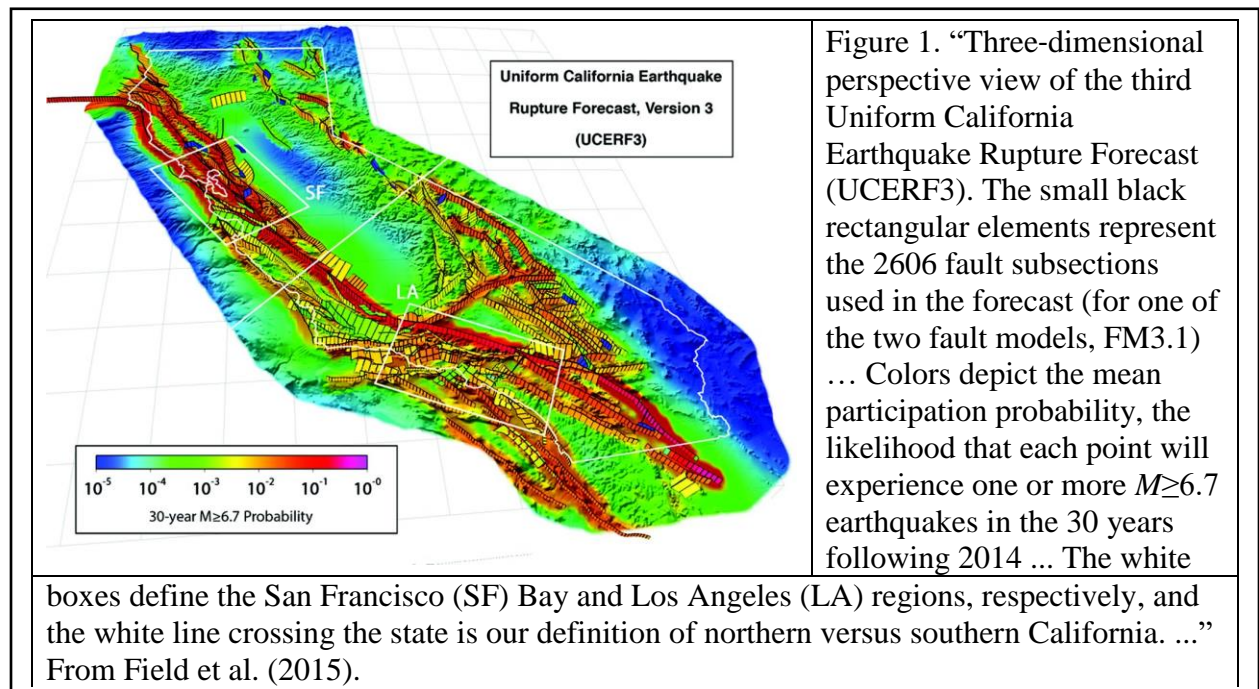
Department of Earth Science and the Earth Research Institute
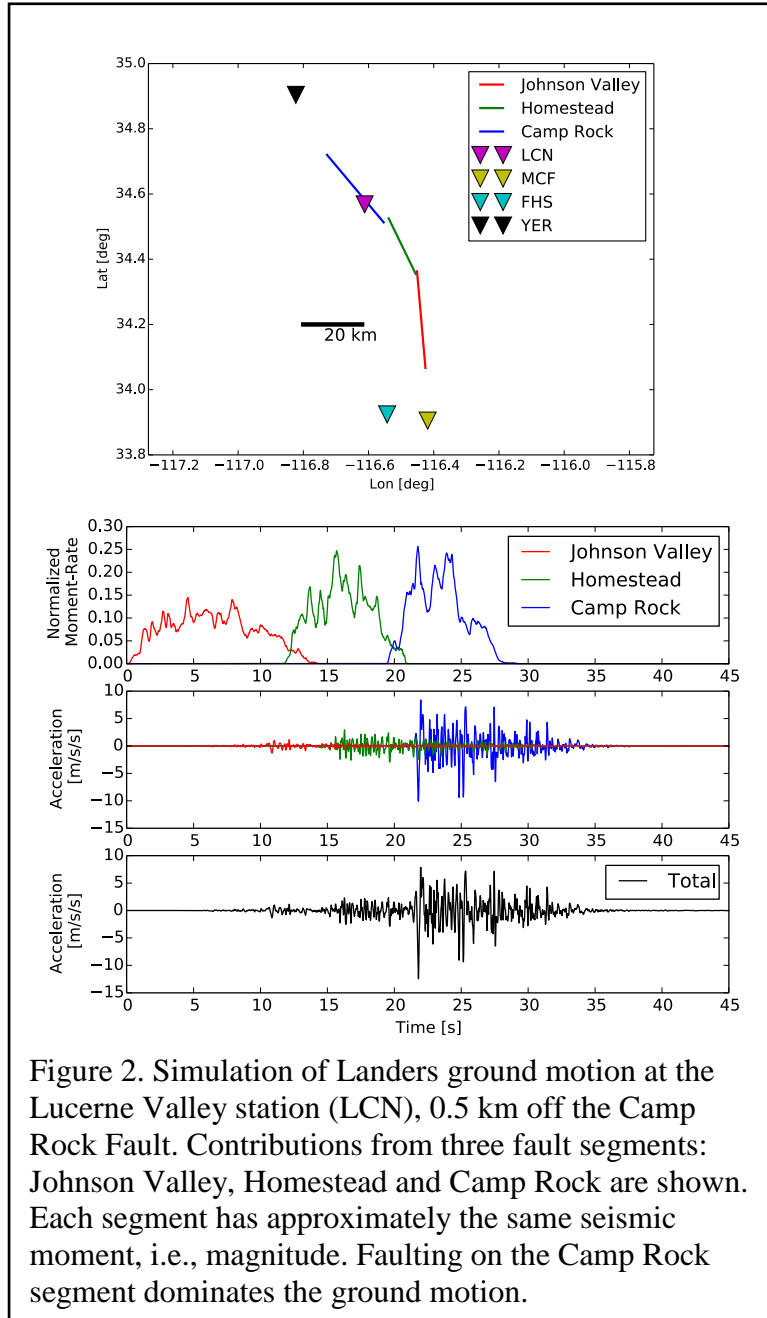University of California, Santa Barbara

Abstract

The 2016 M_W 7.8 Kaikoura earthquake in New Zealand may have involved co-seismic slip on more than 10 distinct faults. We attempt to assess the sequence of rupture on the segments as well as the contribution of the different segments to the recorded ground motion in New Zealand. First, we approximate the segments as points sources to determine the temporal sequence of faulting and to determine the relative contribution to the seismic moment. We reduce the overall number of segments to 10 crustal faults. We invert strong motion, geodetic and teleseismic body and surface wave data to provide a spatio-temporal map of slip and rupture time.

Introduction

Large earthquakes often involve slip on more than one fault. Four notable examples are 1) the 1992 M_W 7.3 Landers, California, earthquake with slip on five different faults; 2) the 2012 M_W 8.6 Indian Ocean earthquake with slip on four faults—three of which are perpendicular to the primary fault; 3) the 2010 M_W 7.1 Darfield, New Zealand, earthquake, with slip on as many as eight segments and 4) the 2010 M_W 7.2 El Mayor–Cucapah, Mexico, earthquake comprised of seven faults. The latest hazard assessment for California (Figure 1) includes ruptures that involve

Figure 1. "Three-dimensional perspective view of the third Uniform California Earthquake Rupture Forecast (UCERF3). The small black rectangular elements represent the 2606 fault subsections used in the forecast (for one of the two fault models, FM3.1) … Colors depict the mean participation probability, the likelihood that each point will experience one or more $M{\geq}6.7$ earthquakes in the 30 years following 2014 ... The white boxes define the San Francisco (SF) Bay and Los Angeles (LA) regions, respectively, and the white line crossing the state is our definition of northern versus southern California. ..." From Field et al. (2015).

Figure 2. Simulation of Landers ground motion at the Lucerne Valley station (LCN), 0.5 km off the Camp Rock Fault. Contributions from three fault segments: Johnson Valley, Homestead and Camp Rock are shown. Each segment has approximately the same seismic moment, i.e., magnitude. Faulting on the Camp Rock segment dominates the ground motion.

multiple faults (Field et al., 2015). If these earthquakes are looked at from great distances (1000's of kilometers), i.e., treated as point sources, there are standard methods for assigning a seismic moment/magnitude. However, when considering the near source ground motion where the largest amplitudes generally occur, there is a fundamental question that needs to be examined. Should near source ground motion be assigned to the magnitude of the closest segment or the magnitude of the entire complex rupture?

As an example, Crempien and Archuleta (2016) computed ground motion based on a kinematic rupture simulation that uses heterogeneous faulting on three segments representing the M 7.3 Landers earthquake in 1992 (Figure 2). The three fault segments are the Johnson Valley fault (on which the rupture starts)—the southern-most segment, the Homestead Fault segment in the middle, and the Camp Rock Fault on which the rupture terminates. The station closest to the overall rupture is Lucerne Valley which is next to the Camp Rock segment. It also had the largest recorded peak ground acceleration (PGA) and peak ground velocity (PGV). The peak ground acceleration is clearly dominated by rupture on the Camp Rock Fault, which has one-third of the total moment—a magnitude of 7.0 compared to 7.3 for the entire earthquake.

2016 Kaikoura Earthquake

The complexity of faulting during the 2016 Kaikouora earthquake is illustrated in Figure 3 (taken from Hamling et al., 2017). At least 10 faults in the Marlborough Fault System (MFS) were activated in this earthquake. Hamling et al. (2017) further modeled it using 19 rectangular

fault segments, with the possibility of a 20th with slip on the Hikurangi subduction zone interface (HSZI) (Figure 3). Whether or not slip occurred on the HSZI that underlies the MFS is an open question (Hamling et al., 2017). Clark et al. (2017) improved on the fit to geodetic data of Hamling et al. (2017) by allowing slip on the Point Kean fault, a crustal thrust fault with coseismic outcrop offshore. In allowing slip on the Point Kean fault they found that the inverted

Figure 3. "The main panel shows the location of the continuous (white triangles) and campaign (red triangles) GPS site. … Labels in all capital letters show the towns and cities of Kaikōura, Wellington, and Nelson, as well as the Cape Campbell region. The dashed black boxes indicate the regions shown by the two panels inset at right. The vector shows the relative plate motion between the Pacific (PAC) and Australian plates (AUS), as indicted in the top left inset. AF, Alpine fault. The beach ball icon denotes the W-phase moment tensor generated by the U.S. Geological Survey (USGS) at the epicentral location.

Bottom right inset: Distribution of relocated aftershocks with $M_w > 3$ occurring in the first 2 weeks after the mainshock. Earthquakes are color coded by moment magnitude. The histogram shows the depth distribution of M_w4.5 and above. Top right inset: Map showing

slip on HSZI decreased. Both studies ignored the contribution of Papatea fault, which produced over 6 meters of uplift, and was interpreted as non-elastic deformation. The contribution of Papatea fault was included in the models of two recent papers (Xu et al., 2018; Wang et al., 2018). Xu et al. (2018) constructed three models with different geometries, using only geodetic observations. Fault slip in their Model I was limited to crustal faults but did not include the Point Kean fault. Model II further included the contribution of HSZI; while Model III included the contribution of Point Kean fault but did not include the HSZI. Xu et al. (2018) indicated that because every model can explain the geodetic observations well, whether slip occurred on the HSZI cannot be answered by the geodetic data alone, as concluded by Hamling et al. (2017) and Clark et al. (2017). In contrast, Wang et al. (2018) did a joint inversion with geodetic

measurements, strong motion and teleseismic body waves. They argued that the rupture of HSZI is required by the seismic data. Their preferred model has about 45% of total seismic moment on the HSZI. It is important to note that Wang et al. (2018) did not include any contribution from the Point Kean fault. A good review of other researchers who have explored the multi-fault Kaikoura earthquake can be found in Chapter 4 of Adams (2018).
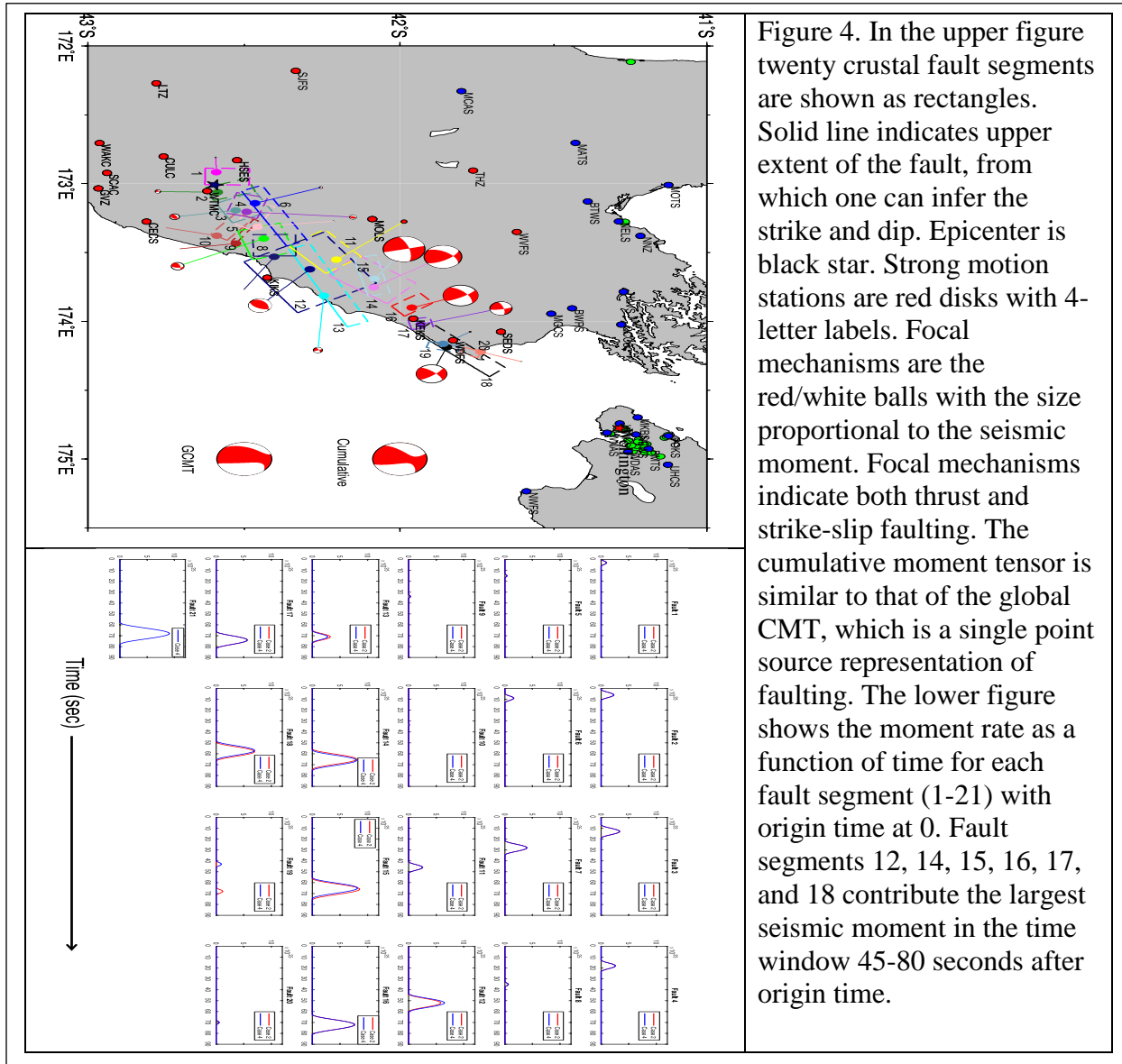

Figure 4. In the upper figure twenty crustal fault segments are shown as rectangles. Solid line indicates upper extent of the fault, from which one can infer the strike and dip. Epicenter is black star. Strong motion stations are red disks with 4-letter labels. Focal mechanisms are the red/white balls with the size proportional to the seismic moment. Focal mechanisms indicate both thrust and strike-slip faulting. The cumulative moment tensor is similar to that of the global CMT, which is a single point source representation of faulting. The lower figure shows the moment rate as a function of time for each fault segment (1-21) with origin time at 0. Fault segments 12, 14, 15, 16, 17, and 18 contribute the largest seismic moment in the time window 45-80 seconds after origin time.

Because so many faults are involved, our first effort is to determine the timing among the faults and the relative seismic moment contribution of each segment, assuming the slip distributions inferred from geodetic observations are correct. We use the slip model of Clark et al. (2017), which includes 21 fault segments. The 21th fault segment is the plate interface. We treat every fault segment as one subevent and model it as a double-couple point source. We fix the point source locations as the centroid locations inferred from the fault slip on the corresponding fault segments, and constrain both centroid time and seismic moment of every

point source using the close-fault strong motion records with the multiple double-couple (MDC) inversion approach (Li et al., 2011; Shao et al., 2011). The slip rate function of each point source is modeled as symmetric cosine function (Ji et al., 2002) with a half duration calculated using the empirical scaling relationship between seismic moment and half duration ($T_h = 2.24 \times 10^{-6} \times M_0^{1/3}$, Ekström et al., 2005).

			H1	H2	HR	HT	CESMD	Rrup
STA	Lat.	Long.	(cm/s/s)	(cm/s/s)	(cm/s/s)	(cm/s/s)	(cm/s)	(km)
CECS	-42.813	173.275	123.12	213.12	284.96	276.80	31.7	27.7
CULC	-42.759	172.803	246.75	336.75	241.90	242.07	33.2	15.6
GVZ	-42.967	173.035	177.71	267.71	112.60	146.64	12.0	37.8
HSES	-42.523	172.83	320.02	50.02	268.69	258.52	29.9	11.8
KEKS	-41.956	173.981	43.85	133.85	1337.88	382.30	79.8	3.0
KIKS	-42.426	173.682	61.43	151.43	200.09	252.09	44.5	0.7
LTZ	-42.782	172.271	260.79	350.79	84.25	67.48	6.0	52.8
MOLS	-42.088	173.257	16.19	106.19	294.90	445.84	14.1	29.5
SCAC	-42.939	172.922	196.19	286.19	268.50	210.43	26.5	34.5
SEDS	-41.672	174.076	37.3	127.3	571.16	746.22	52.8	22.7
SJFS	-42.335	172.18	300.02	30.02	42.71	58.35	7.6	65.1
THZ	-41.762	172.905	354.78	84.78	48.27	38.36	7.2	72.7
WAKC	-42.963	172.705	220.45	310.45	146.63	141.34	17.3	39.8
WDFS	-41.827	174.138	43.53	133.53	769.16	1175.55	83.2	8.5
WTMC	-42.619	173.054	19.45	109.45	943.14	995.19	101.7	0.7
WVFS	-41.620	173.351	12.85	102.85	147.70	149.02	25.9	55.5

Table 1: Strong Motion Stations with maximum values of PGA and PGV

All values in the table are taken from the unprocessed records. H1 and H2 are the original horizontal orientations, which vary from station to station. HR and HT are the radial and transverse orientations as measured from the epicenter. The maximum ground velocity is from the processed records at the Center for Engineering Strong Motion Data (CESMD). Rrup is closest distance to the fault from CESMD.

We select three components of ground motion velocity at 16 close-fault strong motion stations (Table 1) and bandpass filter the signals to periods between 10 s and 90 s. Note that half of the strong motion stations are in the southern end of the rupture where slip on the faults is generally small relative to slip on faults northeast of the hypocenter (Figure 4). In Figure 4, we show the results of two cases. In Case 2 we only investigate the crustal faults, i.e., the point source associated with the 21th fault segment is ignored. In case 4, all fault segments are considered. This study provides a temporal sequence of when the different fault segments contributed to the overall rupture and the relative contribution to the overall seismic moment (Figure 4). For example, the MDC result suggests that strong motion stations south of the hypocenter were mostly affected by the early part (Faults 1-9) of the Kaikoura earthquake, which

was effectively a M_W 7.27 earthquake. The rupture generally unilaterally propagated to the northeast and the rupture of the plate interface occurred from 60 s to 80 s.

To invert for spatio-temporal kinematic parameters we consolidated the 20 crustal fault segments to 10 (Table 2). We further divided them into 3.5 km by 4 km subfaults and simultaneously invert slip, rake angle, rupture initiation time, and the shape of analytic slip rate function of each subfault, using both seismic and geodetic observations. Our seismic data is composed of: i) three components of ground motion velocity at the same 16 stations (Table 1). The velocity time histories are 125 seconds in length and bandlimited to periods between 50 s and 2 s (Figure 5). Note that the horizontal motion has been rotated to radial (R) and transverse (T) components relative to the Kaikuara epicenter; ii) displacement waveforms at 6 high-rate GPS stations (sampling rate 10Hz). A lowpassed filter with a corner of 1.0 Hz has been applied (Figure 6); iii) teleseismic broadband P and SH recordings at 26 stations (Figure 7); iv) long-period (4-6mHz) whole waveforms in vertical and transverse components of 33 stations (Figure 8). The geodetic data include static offsets from 20 continuous GPS sites and 64 campaign sites (Hamling et al., 2017).
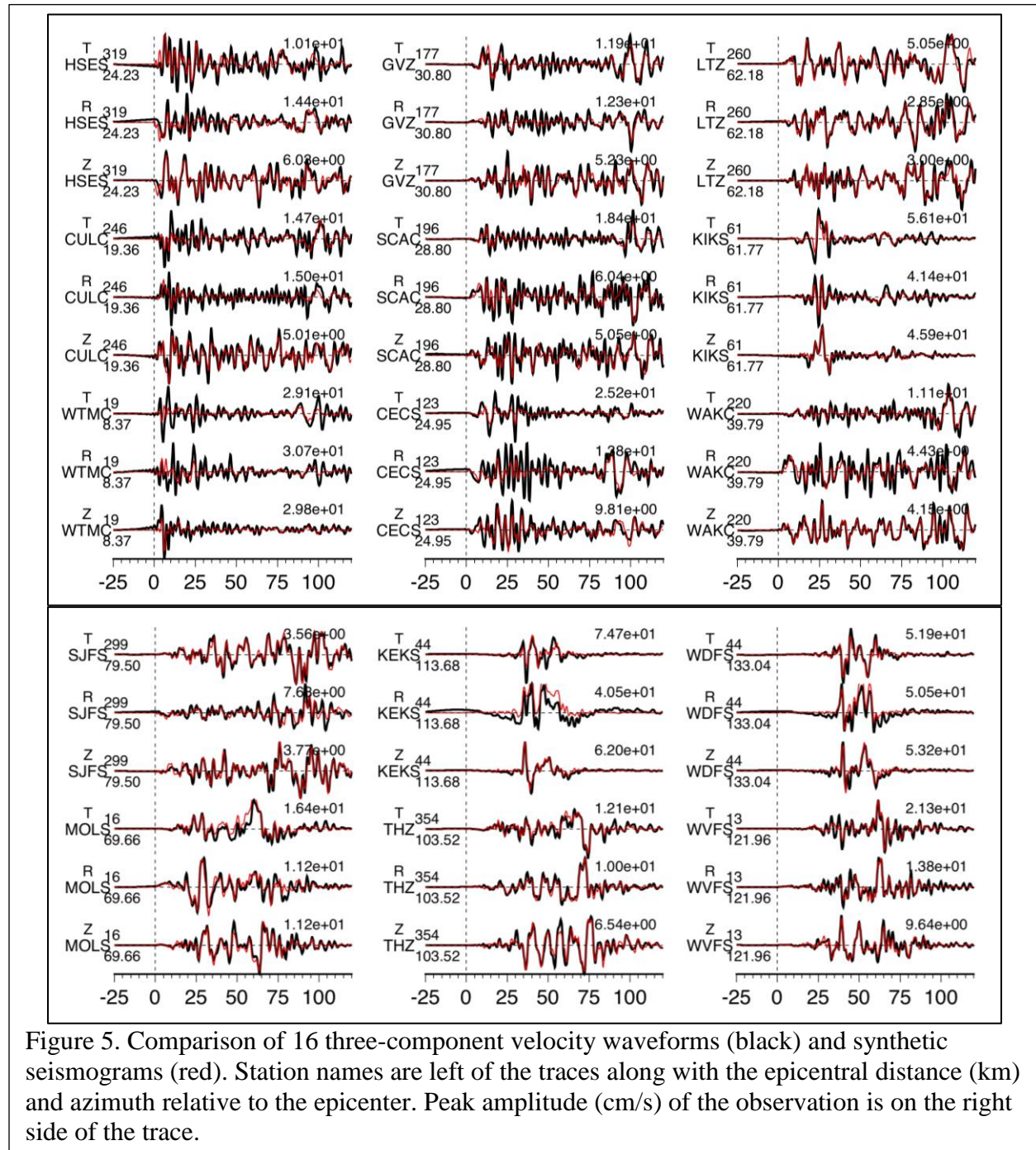
Table 2. Fault Description										
Fault ID	Fault Name Wang et al. (2008)	Length (km)	Width (km)	Strike°/ dip°/rake°*	M_0 (Nm)	Mw	Ave. Slip* (m)	Ave. Rise time* (s)	Ave. Slip rate* (m/s)	Ave. Stress* (MPa)
1	Humps-west	21	20	77/65/(-8)	5.6×10^{18}	6.5	1.2	5.1	0.4	3.3
2	Humps-east	21	20	255/70/(166)	7.7×10^{19}	7.2	4.9	5.0	1.2	8.0
3	Leader	21	24	195/50/(78)	2.8×10^{19}	6.9	3.1	4.4	0.8	7.6
4	Hundalee-west	28	32	230/45/(85)	8.0×10^{19}	7.2	3.8	4.0	1.1	4.8
5	Whites	24.5	32	172/45/(86)	3.3×10^{19}	7.0	1.9	2.9	0.8	5.5
6	Point Kean	28	40	243/35/(126)	2.3×10^{19}	7.5	5.0	4.8	1.6	9.5
7	Papatea	21	32	172/50/(61)	1.1×10^{20}	7.3	7.8	6.0	1.4	10.7
8	Jordan_ Kekerengu	59.5	32	223/50/(170)	2.5×10^{20}	7.6	7.5	4.9	1.9	10.0
9	Kekerengu	21	32	242/50/(161)	1.5×10^{20}	7.4	8.7	6.6	1.8	15.6
10	Needles	35	32	222/50/(162)	1.1×10^{20}	7.3	5.4	5.0	1.3	12.4

* rake angle, slip, rise time, slip, stress drop are average values weighted by fault slip (Ji et al., 2002). The slip rate at individual subfault is simply defined as ratio of fault slip and rise time. Note that the average slip rate is larger than the ratio of average fault slip and average rise time. The stress drop is in the direction of average rake angle.

As shown in Figures 5-8, synthetic seismograms predicted with our preliminary model generally match data well. The fit to the strong motion and high rate GPS data is good for both amplitude and duration though there are some noticeable exceptions such as the peak amplitude of the transverse (T) component of KEKS and WTMC (Figure 5), and the polarity discrepancy at vertical component (Z) of station MRBL (Figure 6). The fit to the teleseismic P and SH waves and the long-period surface waves is better.

The slip distribution of the preliminary model is shown in Figure 9. We also illustrate the contribution of each fault segment and its individual moment rate function in Figure 10. All of the moment rate functions are scaled to the same maximum in order to show the relative

contribution from the 10 faults. Zero time is the origin time for the earthquake. The cumulative moment rate function is shown in Figure 11. The fault parameters of our preliminary slip model are summarized in Table 2. Initial rupture on the Humps-west fault is equivalent to M_W 6.5 (Table 2). In Figure 12 the sequence of slip is shown as a series of snapshots of the slip

Figure 5. Comparison of 16 three-component velocity waveforms (black) and synthetic seismograms (red). Station names are left of the traces along with the epicentral distance (km) and azimuth relative to the epicenter. Peak amplitude (cm/s) of the observation is on the right side of the trace.

accumulated in 10 s intervals. One of the most interesting features is the jump to the northern part of the Kekerengu fault around 50-60 seconds. The rupture then proceeds southwest on the Kekerengu fault and then moves northeast after about 10 seconds. It reveals that 2016 Kaikuara earthquake has a complex rupture process.

7
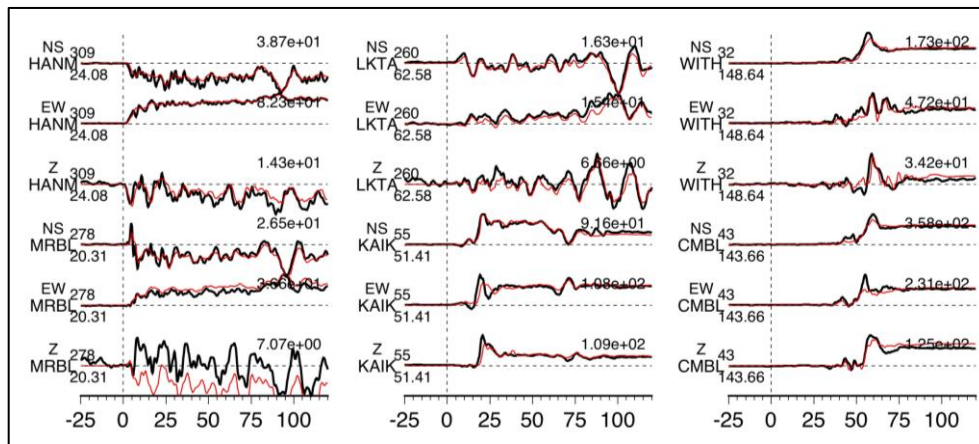
Figure 6. Comparison of synthetics (red) with data (black) of continuous, high-rate GPS low-passed filtered with a 1.0 s corner. Units are cm, shown on the right of each trace. On the left is the station code, component, azimuth and distance (km) from epicenter. The station MRBC is close to the end of the Humps fault which we approximated as a straight fault but may be curved. All other fits are good including the static offset.

Rupture Process:

1. Although we let rupture initiate at south dipping Humps-west fault, most inverted fault slip occurred on north-dipping Humps-east fault as right-lateral strike slip in the first 25 s and unilaterally propagated to the northeast. The rupture on this segment ended with a transpressional motion on the west-dipping Leaders fault. The rupture of the Humps-Leaders fault system is associated with relatively high stress drop of 7.6-8.0 MPa as compared with global average 3-4 MPa (Kanamori and Anderson, 1975; Allmann and Shearer, 2009).

2. About 12 s after the event started, rupture on the Hundalee fault initiated. The rupture of this fault segment is nearly pure thrust with an average rake angle of 85°. The rupture of this fault segment reached its peak moment rate around 25-30 s and ceased sharply at 35 s. The cumulative seismic moment is 8.0×10^{19} Nm (M_W 7.3). Rupture on Whites fault initiated at about 25 s and continued about 40 s— again with a pure thrust focal mechanism. Though the cumulative seismic moment is still significant (3.3×10^{19} Nm, M_W 7.0), this rupture duration is much longer than a typical rupture of this magnitude (~14 s). The stress drop on these two segments is around 5 MPa.

3. Rupture of Point Kean fault initiated at 25 s on the shallow portion of the fault plane with an oblique focal mechanism (average rake angle of 126°). The total rupture duration is about 50 s and the cumulative seismic moment is 2.3×10^{20} Nm (M_W 7.5). Note that from 60 to 80 s, the rupture is limited to subfaults with depth >20 km. The cumulative seismic moment during this period is 1.2×10^{20} Nm (M_W 7.4).

4. The rupture of Jordan thrust- Kekerengu-Needles fault, which we modeled using three fault segments, might start as earlier as 25 s from its southwest end. However, the major asperity extending from roughly 70 km to 150 km northeast of the Kaikuara epicenter failed first in the middle on the shallow portion of Kekerengu fault, near the strong motion station KEKS,

at 53 s. This subevent sharply ceases at 62 s. The cumulative seismic moment during this period is 1.7×10^{19} Nm (M_W 6.8), consistent with previous result of Holden et al. (2017). The southwest edge of this asperity rupture initiated at about 60 s and gradually propagated to the northeast. About half of the total seismic moment occurred on these three fault segments.
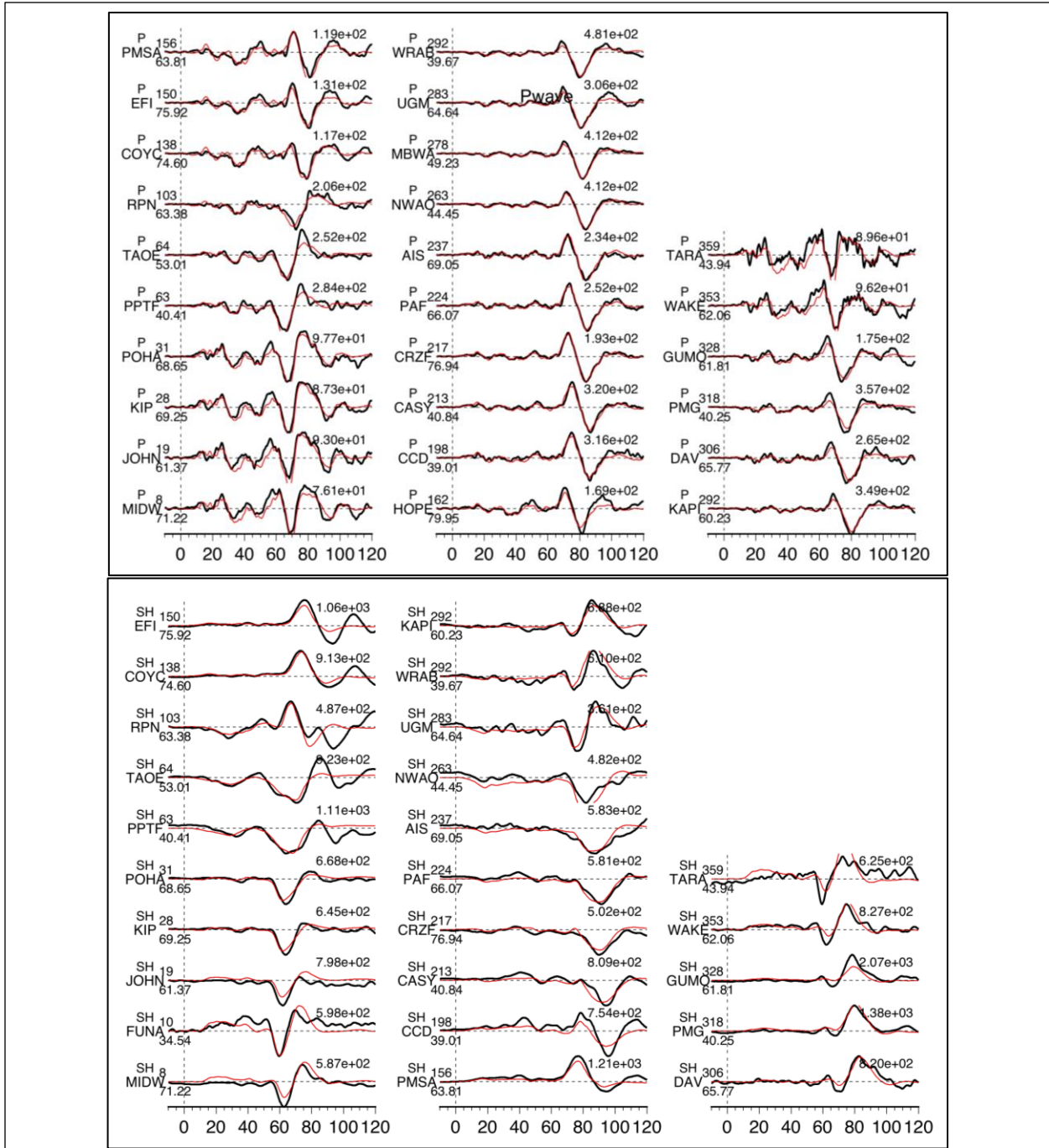

Figure 7. Displacement of P and SH waves vs time (s). Data in black and synthetics in red. Left of each trace is the station code. Upper number is the azimuth relative to the epicenter and lower number is the angular distance in degrees. On the right is the maximum amplitude (units are 10^{-6}m) of the observation.
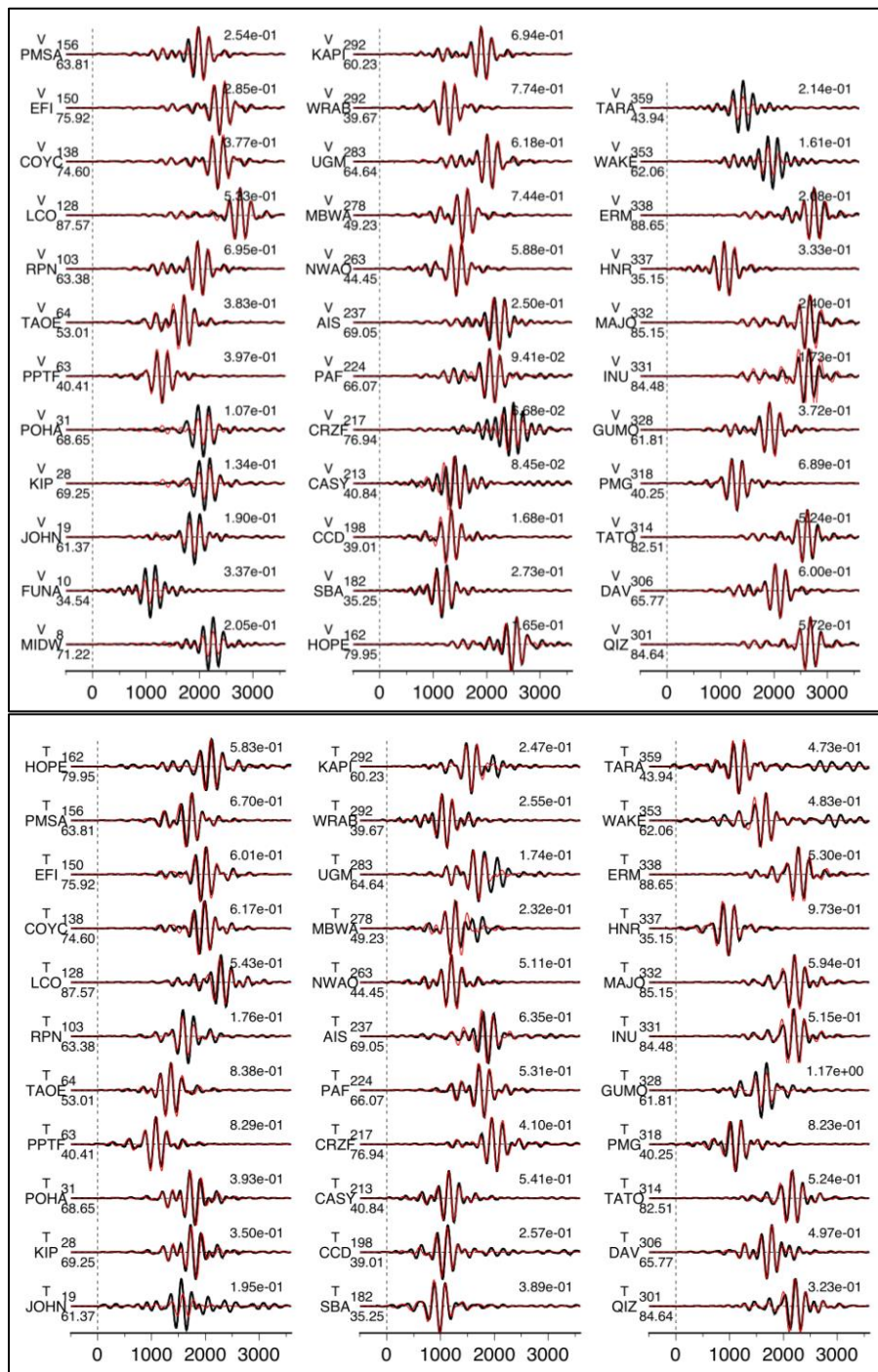
Figure 8. Long period surface waves (vertical-upper and transverse-lower) vs time (s). Data in black and synthetics in red. Left of each trace is the station code. Upper number is the azimuth relative to the epicenter and lower number is the angular distance in degrees. On the right is the maximum amplitude (10^{-3}m) of the observation.
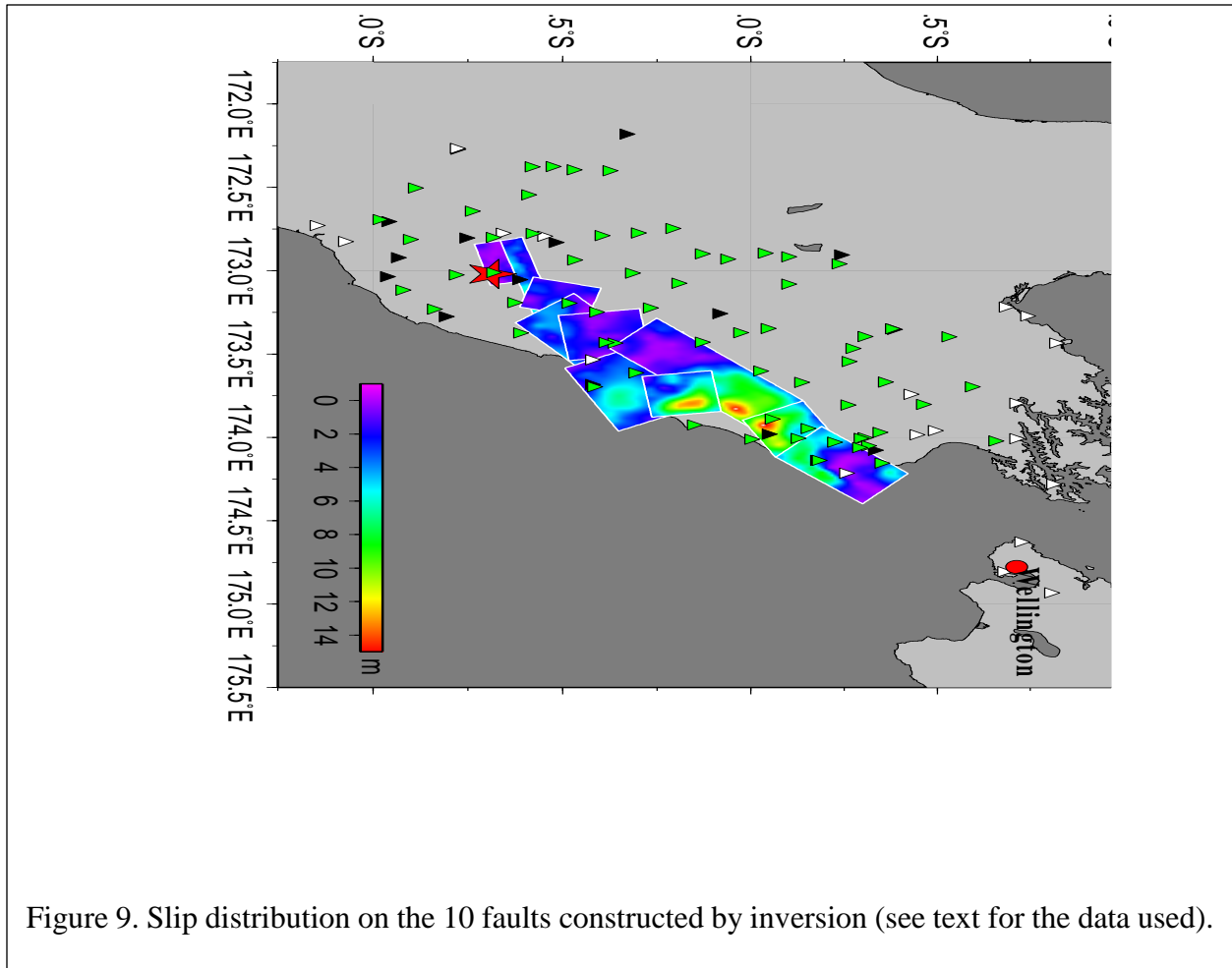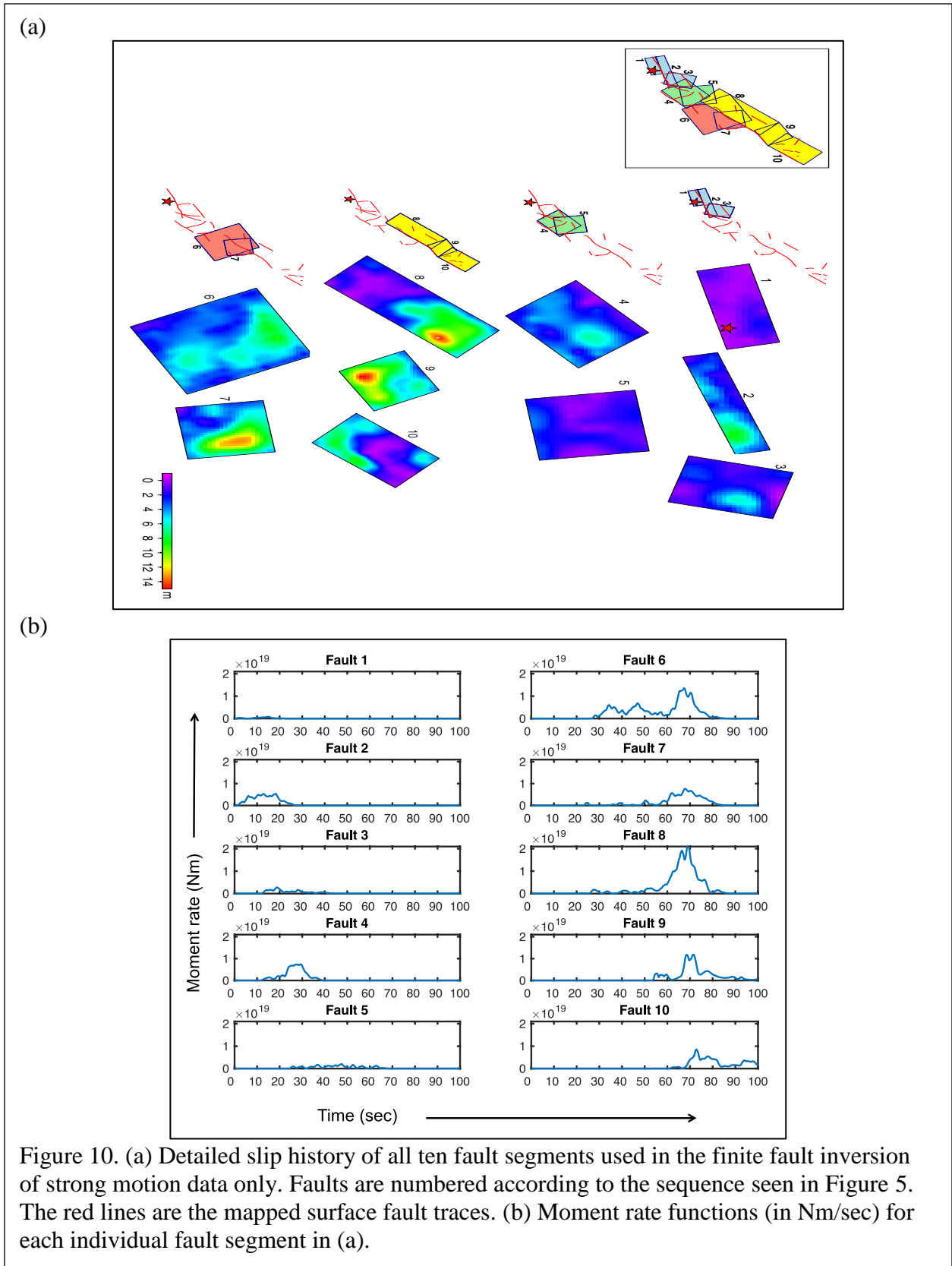
Figure 9. Slip distribution on the 10 faults constructed by inversion (see text for the data used).

5. The rupture on the Papatea fault has an oblique focal mechanism with average rake angle of 61°. The cumulative seismic moment is 1.0×10^{20} Nm, equivalent to a moment magnitude 7.3. Both the average rake angle and seismic moment are similar to the results of Xu et al. (2018) using both GPS and INSAR data. Their estimates are 50° and 1.3×10^{20} Nm, respectively in fault model I. It is noteworthy that the Model I didn't consider the contribution of the Point Kean fault. While the rupture initiation of Papatea fault is poorly constrained, about 90% of its total seismic moment occurred between 55 s and 85 s.

A scalar summation of the seismic moments of 10 fault segments yields an estimate of total seismic moment of 1.08×10^{21} Nm (M_W 8.0).

Table 3: Comparison of the centroid moment tensor of this study and GCMT								
Solution	M_0	CLVD	T axis		N axis		P axis	
	$(10^{20}$ Nm)		plunge	azimuth	plunge	azimuth	plunge	azimuth
GCMT	6.7	31%	56°	225°	25°	360°	21°	100°
This study	7.2	27%	54°	212°	7°	33°	12°	105°

(a)

(b)

Figure 10. (a) Detailed slip history of all ten fault segments used in the finite fault inversion of strong motion data only. Faults are numbered according to the sequence seen in Figure 5. The red lines are the mapped surface fault traces. (b) Moment rate functions (in Nm/sec) for each individual fault segment in (a).

Including the GPS and teleseismic data, rather than inversion of strong motion data only, leads to larger slip and overall larger seismic moment. This is seen in Figure 12 where we compare the overall moment rate functions of the two models. The cumulative moment rate shows that the Kaikoura earthquake generated about two thirds of the seismic moment after 60 seconds. However, many of the largest accelerations are to the south of the hypocenter.
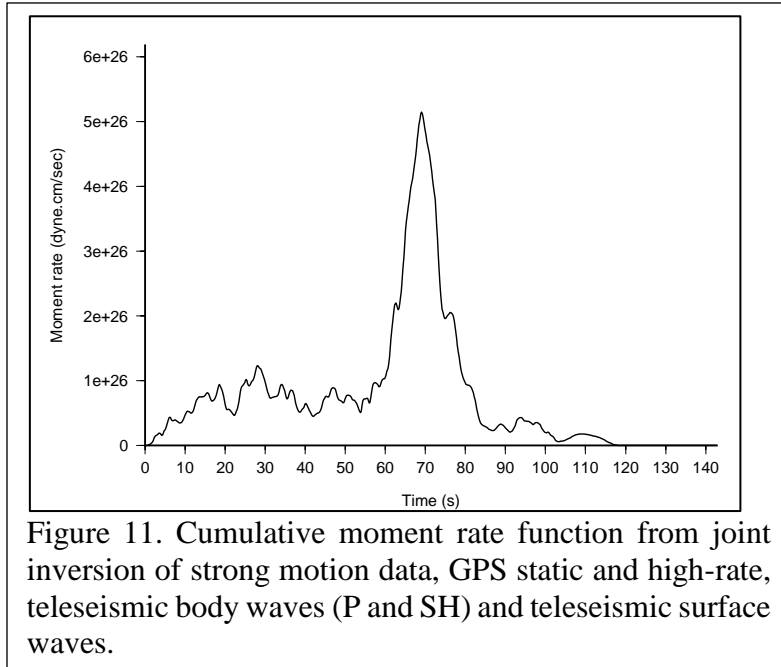
Figure 11. Cumulative moment rate function from joint inversion of strong motion data, GPS static and high-rate, teleseismic body waves (P and SH) and teleseismic surface waves.

Discussion

The tensor summation of these sub-sources leads to our estimate of the centroid moment tensor (Table 3), which has a scalar seismic moment of 7.2×10^{20} Nm (M_W 7.9). This is nearly identical to the GCMT estimate of 6.7×10^{20} Nm but one third smaller than the value of scalar summation. Hence, for such complex rupture processes, point source moment tensor inversion such as GCMT often underestimates the cumulative scalar seismic moment of a large earthquake.

With many parameters being used in finite fault inversions to represent the earthquake process during, some of them are inevitably correlated. For example, Ji et al. (2003) noticed the trade-off between the rupture initiation time and starting time of each subfault. The time of peak slip rate (peak time), which can be represented as a summation of rupture initiation time and starting time, is often better constrained. We show the peak time and hypocenter distance at the center of every subfault as a red dot in Figure 13. It reveals that the migration speed of the peak time from the hypocenter is clearly less than 2 km/s, consistent with previous studies. However, the local rupture velocity varies significantly. In particular, the subfaults with hypocenter distances from ~70 km to ~130 km (60 km), involving five fault segments—Point Kean, Jordan_Kekerengu, Kekerengu, Needles, Papatea—with different focal mechanisms, reach the peak slip rate all around 70 s. This is associated with the largest moment rate peak in cumulative moment rate function (Figure 11).

In this study, we present a slip model that matches the available near and far field observations without a contribution from the plate interface. However, whether the plate interface ruptured during the Kaikoura earthquake is still a question that remains unresolved. Note that the rupture of Point Kean fault during the period of 60 to 80 s is limited to subfaults with depths greater than 20 km, about 5 km above the plate interface. The cumulative seismic moment during this period is 1.2×10^{20} Nm (M_W 7.4), which is about 11% of the total seismic moment. The rupture of this slip patch dominates the later phase of station MOLS, which is the closest strong motion station to this slip patch. However, as shown in Wang et al. (2018), slip on plate interface can also match this record.
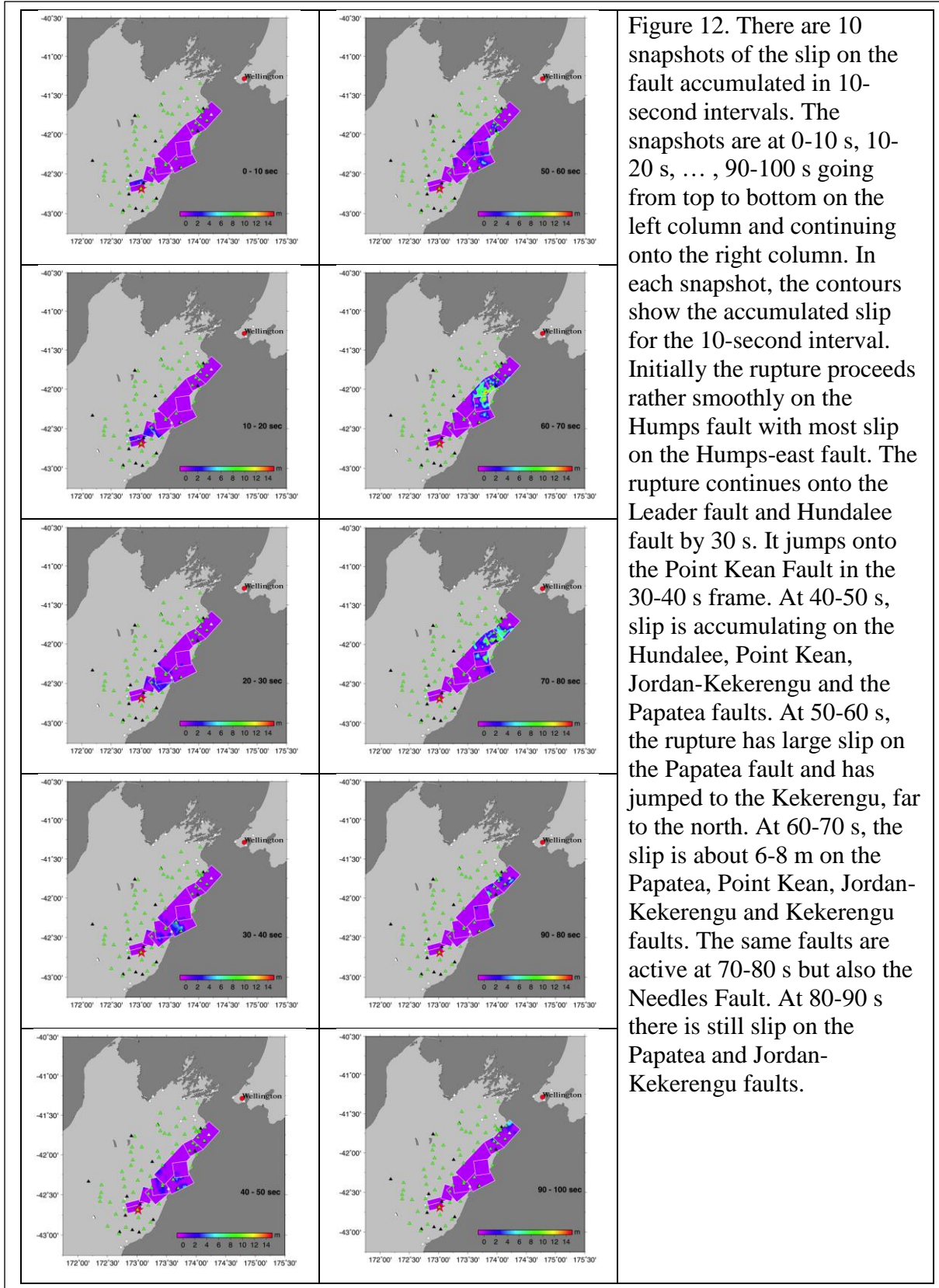
Figure 12. There are 10 snapshots of the slip on the fault accumulated in 10-second intervals. The snapshots are at 0-10 s, 10-20 s, … , 90-100 s going from top to bottom on the left column and continuing onto the right column. In each snapshot, the contours show the accumulated slip for the 10-second interval. Initially the rupture proceeds rather smoothly on the Humps fault with most slip on the Humps-east fault. The rupture continues onto the Leader fault and Hundalee fault by 30 s. It jumps onto the Point Kean Fault in the 30-40 s frame. At 40-50 s, slip is accumulating on the Hundalee, Point Kean, Jordan-Kekerengu and the Papatea faults. At 50-60 s, the rupture has large slip on the Papatea fault and has jumped to the Kekerengu, far to the north. At 60-70 s, the slip is about 6-8 m on the Papatea, Point Kean, Jordan-Kekerengu and Kekerengu faults. The same faults are active at 70-80 s but also the Needles Fault. At 80-90 s there is still slip on the Papatea and Jordan-Kekerengu faults.
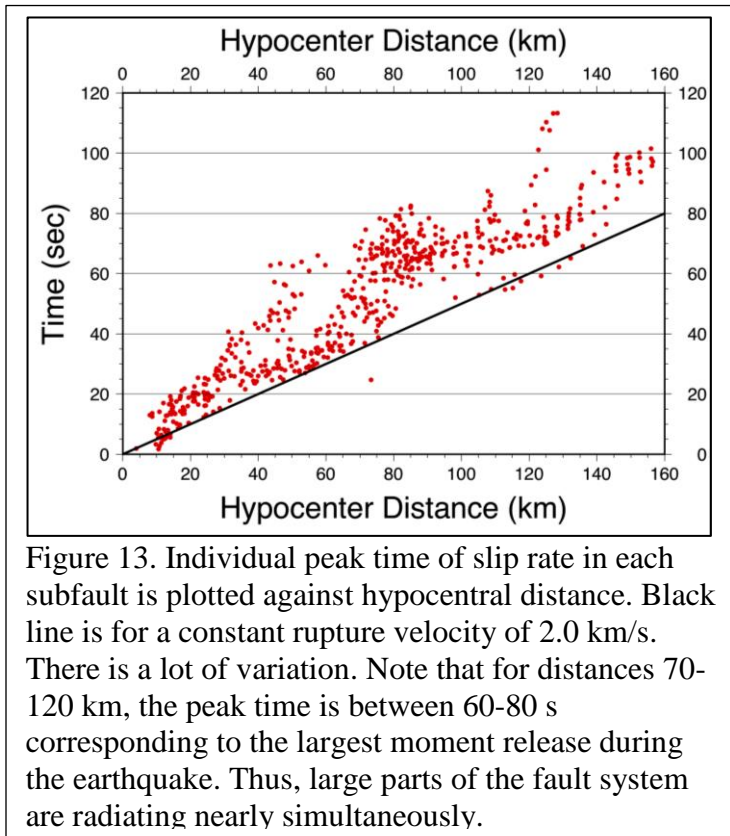
Figure 13. Individual peak time of slip rate in each subfault is plotted against hypocentral distance. Black line is for a constant rupture velocity of 2.0 km/s. There is a lot of variation. Note that for distances 70-120 km, the peak time is between 60-80 s corresponding to the largest moment release during the earthquake. Thus, large parts of the fault system are radiating nearly simultaneously.

The rupture Papatea fault produced up to 8 m uplift. But Holden et al. (2017) noted that it has relatively minor contribution to local waveforms despite its large slip. As shown in Figure 10b, ~90% of the seismic moment occurred within the time window of 55 s to 85 s, when rupture of the deep portion of the Point Kean fault, Jordan_Kekerengu fault, Kekerengu fault and Needles fault also reach their peak moment rates. The cumulative seismic moment of the rupture on these four fault segments during this period is 5.4×10^{20} Nm, 5-6 times of the Papatea fault rupture. Further considering the fact that north of Kaikoura, all strong motion and high rate GPS stations locate west of the Kaikoura fault zone. Therefore, these stations are more sensitive to the rupture of the four fault segments than Papatea fault segment. It is then not surprising that it was difficult to uniquely resolve rupture of the Papatea fault segment using only strong motion observations (Holden et al., 2017).

Conclusions

The M_W 7.8 Kaikoura earthquake is a complex event involving slip on at least 10 faults. Inversion that joined the seismic waveforms of strong motion, high-rate GPS, and teleseismic observations with GPS static field observations shows multiple faults simultaneously rupturing. The results also indicate that strong motion is not controlled by the fault segments with the largest slip. For example, the Papatea fault, which has large slip over a long time, has little effect on strong motion. Most of the seismic moment is released in a 30 second window (55-85s) on five faults: Point Kean, Jordan_Kekerengu, Kekerengu, Needles, Papatea, all of which are well north of the hypocenter. Near the hypocenter, the Humps and Leader faults produce smaller amounts of slip but with significant stress drop, ~8 MPa. This leads to high amplitude ground motion in the southern part. However, the combined seismic moment is only 1.06×10^{20} Nm (M_W 7.3, 10% of total moment).

References

Adams, M.N., (2018), Subject-oriented finite fault inversions and their applications, PhD dissertation, University of California, Santa Barbara.

Clark, K.J., Nissen, E.K., Howarth, J.D., Hamling, I.J., Mountjoy, J.J., Ries, W.F., Jones, K., Goldstein, S., Cochran, U.A., Villamor, P., Hreinsdóttir, S., Litchfield, N.J., Mueller, C., Berryman, K.R. and Strong, D.T. (2017), Highly variable coastal deformation in the 2016 M_W7.8 Kaikōura earthquake reflects rupture complexity along a transpressional plate boundary. *Earth and Planetary Science Letters*, **474**, 334–344. http://doi.org/10.1016/j.epsl.2017.06.048.

Crempien, J.G.F. and Archuleta, R.J., (2015), UCSB method for simulation of broadband ground motion from kinematic earthquake sources, *Seismological Research Letters, **86**,* 61-67.

Ekström, G., Dziewoński, A.M., Maternovskaya, N.N. and Nettles, M. (2005). Global seismicity of 2003: Centroid-moment-tensor solutions for 1087 earthquakes. *Physics of the Earth and Planetary Interiors*, **148**(2–4), 327–351. http://doi.org/10.1016/j.pepi.2004.09.006.

Field, E. H., Biasi, G.P., Bird, P., Dawson, T.E., Felzer, K.R., Jackson, D.D., Johnson, K.M., Jordan, T.H., Madden, C., Michael, A.J., Milner, K.R., Page, M.T., Parsons, T., Powers, P.M., Shaw, B.E., Thatcher, W.R., Weldon, R.J., and Zeng, Y. (2015), Long-term time-dependent probabilities for the Third Uniform California Earthquake Rupture Forecast (UCERF3), *Bull. Seismol. Soc. Am.* **105**, 511-543, DOI: 10.1785/0120140093.

Hamling, I.J., Hreinsdóttir, S., Clark, K., Elliott, J. , Liang, C., Fielding, E., Litchfield, N., Villamor, P., Wallace, L. , Wright, T.J., D'Anastasio, E., Bannister, S., Burbidge, D., Denys, P., Gentle, P., Howarth, J., Mueller, C., Palmer, N., Pearson, C., Power, W., Barnes, P., Barrell, D.J.A., Van Dissen, R., Langridge, R., Little, T., Nicol, A., Pettinga, J., Rowland, J. and Stirling M. (2017), Complex multifault rupture during the 2016 Mw 7.8 Kaikoura earthquake, New Zealand, *Science* 10.1126/science.aam7194.

Holden, C., Kaneko, Y., D'Anastasio, E., Benites, R., Fry, B. and Hamling, I.J. (2017). The 2016 Kaikōura earthquake revealed by kinematic source inversion and seismic wavefield simulations: Slow rupture propagation on a geometrically complex crustal fault network. *Geophysical Research Letters*, **44**(22), 11,320-11,328. http://doi.org/10.1002/2017GL075301.

Ji, C., Wald, D.J. and Helmberger, D.V. (2002), Source description of the 1999 Hector Mine, California, earthquake, part I: Wavelet domain inversion theory and resolution analysis, *Bulletin Seismological Society of America,* **92**, 1192-1207.

Li, X.Y., Shao, G. and Ji, C. (2011), Multiple double-couple analysis for M6-7 earthquakes, *SCEC 2011 Annual Meeting*.

Shao, G.F., Li, X.Y., Ji, C. and Maeda, T. (2011), Focal mechanism and slip history of the 2011 Mw 9.1 off the Pacific coast of Tohoku earthquake, constrained with teleseismic body and surface waves. *Earth Planets Space* **63**, 559-564.

Wang, T., Wei, S., Shi, X., Qiu, Q., Li, L., Peng, D., Weldon, R.J. and Barbot, S. (2018), The 2016 Kaikōura earthquake: Simultaneous rupture of the subduction interface and overlying faults. *Earth and Planetary Science Letters*, **482**, 44–51. http://doi.org/10.1016/j.epsl.2017.10.056.

Xu, W., Feng, G., Meng, L., Zhang, A., Ampuero, J.P., Bürgmann, R. and Fang, L. (2018), Transpressional rupture cascade of the 2016 Mw7.8 Kaikoura earthquake, New Zealand. *Journal of Geophysical Research: Solid Earth*, **123**, 2396–2409. https://doi.org/10.1002/2017JB015168.